Chemical Science

ROYAL SOCIETY OF CHEMISTRY

EDGE ARTICLE

View Article Online
View Journal | View Issue

Cite this: *Chem. Sci.*, 2020, **11**, 5503

All publication charges for this article have been paid for by the Royal Society of Chemistry

Received 21st February 2020
Accepted 8th May 2020

DOI: 10.1039/d0sc01045f

rsc.li/chemical-science

A bioinspired molybdenum–copper molecular catalyst for CO_2 electroreduction†

Ahmed Mouchfiq,[a] Tanya K. Todorova,[a] Subal Dey,[ab] Marc Fontecave *[a] and Victor Mougel *[b]

Non-noble metal molecular catalysts mediating the electrocatalytic reduction of carbon dioxide are still scarce. This work reports the electrochemical reduction of CO_2 to formate catalyzed by the bimetallic complex $[(bdt)Mo^{VI}(O)S_2Cu^{I}CN]^{2-}$ (bdt = benzenedithiolate), a mimic of the active site of the Mo–Cu carbon monoxide dehydrogenase enzyme (CODH2). Infrared spectroelectrochemical (IR-SEC) studies coupled with density functional theory (DFT) computations revealed that the complex is only a pre-catalyst, the active catalyst being generated upon reduction in the presence of CO_2. We found that the two-electron reduction of $[(bdt)Mo^{VI}(O)S_2Cu^{I}CN]^{2-}$ triggers the transfer of the oxo moiety to CO_2 forming CO_3^{2-} and the complex $[(bdt)Mo^{IV}S_2Cu^{I}CN]^{2-}$ and that a further one-electron reduction is needed to generate the active catalyst. Its protonation yields a reactive $Mo^{V}H$ hydride intermediate which reacts with CO_2 to produce formate. These findings are particularly relevant to the design of catalysts from metal oxo precursors.

Introduction

The development of efficient and selective catalysts for the electrochemical reduction of carbon dioxide is a key step to the sustainable production of carbon-based chemicals. Molecular catalysts mediating the two-electron/two-proton reduction of CO_2 to carbon monoxide (CO) or formic acid (HCOOH) with high activity and selectivity have been identified.[1–3] Their molecular nature enables providing key structural and mechanistic information to rationally design more complex heterogeneous catalysts.[4–13] However, efficient molecular catalysts for CO_2 reduction based on non-noble metals are still scarce.[2,3] Among them, Ni-cyclams,[14,15] Co phthalocyanine and Fe-porphyrins,[16,17] have been discovered decades ago and only a few new members were recently reported, namely $Mn(bpy)(CO)_3Br$,[18] Fe-quaterpyridine,[19] $Fe_4N(CO)_{12}$ [20] and Co diphosphine complexes.[21,22] Interestingly, the great majority of these catalysts perform CO_2 reduction to CO, and only very few, such as CoCp(diphosphine)[21] and $Fe_4N(CO)_{12}$ [23] complexes generate formic acid as the major product.

Enzymatic active sites constitute a great source of inspiration to expand this family of non-noble metal catalysts.[24] Metal complexes replicating features of the active sites of metalloenzymes promoting CO_2 transformation can be conceived in a so-called bioinspired approach. In that context, we had synthesized a series of dithiolene ligands mimicking the molybdopterin cofactor (MPT, shown in Fig. 1) in formate dehydrogenases (FDH) enzymes chelating the metal ion (Mo, W) in a bis(dithiolene) complex with its two sulfur atoms.[25–29] One of the corresponding Mo complexes was shown to be the first example of a FDH mimic displaying catalytic activity for the conversion of CO_2 into formic acid under photochemical conditions.[25] The Ni analogue with the same dithiolene ligand also proved active for CO_2 electroreduction to formic acid, showing high faradaic yields.[30,31] These complexes, in which the Ni ion is coordinated by S atoms exclusively, are also reminiscent of the Ni active site of the Ni–Fe CO-dehydrogenase (CODH1), catalyzing the CO_2-to-CO interconversion.[32]

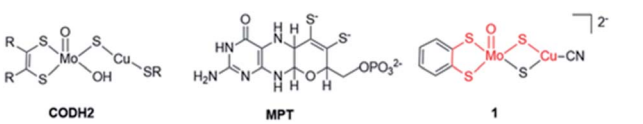

Fig. 1 Active site of CODH2 from *O. carboxidovorans* (left), molybdopterin (MPT, centre) and structure of $[(bdt)Mo(O)S_2CuCN]^{2-}$, complex **1** (right) (MoCu–CODH backbone is highlighted in red in complex **1**).

[a]*Laboratoire de Chimie des Processus Biologiques, UMR 8229 CNRS, Collège de France, Sorbonne Université, 11 Place Marcelin Berthelot, 75231 Paris Cedex 05, France. E-mail: marc.fontecave@college-de-france.fr*

[b]*Department of Chemistry and Applied Biosciences, ETH Zürich, Vladimir Prelog Weg 1, CH-8093 Zürich, Switzerland. E-mail: mougel@inorg.chem.ethz.ch*

† Electronic supplementary information (ESI) available: UV-Vis, NMR and IR spectra of **1**; electrochemical characterizations of **1**, along with catalytic studies; SEM images and EDS spectra of GC electrodes before and after CPE of **1**; electrochemical characterizations of $[Mo(O)(bdt)_2][Et_4N]_2$, along with catalytic studies; structural parameters, IR frequencies, and frontier molecular orbitals of **1** and intermediates; *xyz* coordinates of all intermediates. See DOI: 10.1039/d0sc01045f

Herein, we report the investigation of the electrocatalytic properties of a complex mimicking the active site of the second class of CO-dehydrogenase (CODH2) (Fig. 1). As opposed to CODH1 which functions reversibly, CODH2 has so far been shown to catalyze only CO oxidation to CO_2 and not the reverse reaction, but reasons for this irreversibility are still unclear.[24] Structural characterization of CODH2 from *Oligotropha carboxidovorans* has revealed a heterobimetallic Mo–Cu active site in which the two ions are bridged by a sulfide ion, the Mo ion also being coordinated by the MPT ligand and an oxo/hydroxo moiety (Fig. 1).[33] This metal cofactor has led to the synthesis of a number of biomimetic Mo–Cu complexes, but none of them had been reported to show catalytic activity for CO_2 reduction.[34–38]

In this work, we have performed in-depth investigations of the CO_2 electroreduction catalytic activity of one of these complexes,[38] $[(bdt)Mo^{VI}(O)S_2Cu^{I}CN]^{2-}$, **1**, (bdt = benzenedithiolate), in which Mo and Cu ions are connected by two μ_2-sulfide ligands and the MPT ligand is mimicked by the bdt ligand chelating the Mo ion. While mimicking the structure of CODH2 active site, complex **1** reproduces the function of FDH, catalyzing CO_2 reduction with a high selectivity for formate production. We demonstrate, using infrared spectroelectrochemical (IR-SEC) studies coupled with density functional theory (DFT) calculations that complex **1** is only a pre-catalyst, the active catalyst being formed after reduction and deoxygenation in the presence of CO_2.

Results

Synthesis and characterization of $[(bdt)Mo^{VI}(O)S_2Cu^{I}CN]^{2-}$, (1)

Complex **1** was synthesized following an adapted synthetic procedure from Tatsumi *et al.*[38] and present identical NMR, UV-visible and FTIR spectroscopic signatures to previously reported ones (Fig. S1–S3†). However, the cyclic voltammogram (CV) at 50 mV s^{-1} of **1** under strict anaerobic conditions in argon-saturated CH_3CN using tetrabutylammonium hexafluorophosphate ($TBAPF_6$) supporting electrolyte and glassy carbon (GC) working electrode differed significantly from that published in ref. 38. While the latter exhibited two quasi-reversible waves at $E_{1/2} = -2.02$ V and -1.23 V *vs.* $Ag/AgNO_3$ both originally assigned to one-electron Mo-based redox processes, we only observed a single quasi-reversible process at $E_{1/2} = -2.02$ V *vs.* $Ag/AgNO_3$, (or -2.07 V *vs.* Fc/Fc^+; unless stated otherwise, all potentials in the text below are *vs.* Fc/Fc^+) (Fig. S4 and S5†). In our hands, we noticed the appearance upon exposure of the electrochemical cell containing complex **1** to air of an additional process at -1.22 V *vs.* Fc/Fc^+ (corresponding to the wave at -1.23 V *vs.* $Ag/AgNO_3$ [38]) (Fig. S4†). This CV change proved reversible, as witnessed by the disappearance of this signal after 30 min degassing of the solution with Ar, while the signal at -2.07 V remained unchanged. Therefore, we assigned this signal to O_2 reduction and argue that the previously reported CV[38] reflected a contamination of the electrochemical cell with air (Fig. S4†).

Determination of the number of electrons associated to the redox process at $E_{1/2} = -2.07$ V (Fig. S6 and S7†) by using chronoamperometry in a stationary regime at a carbon microelectrode shows that this process corresponds to a two-electron reduction of complex **1**. We tentatively assigned it to a Mo^{VI}/Mo^{IV} process according to eqn (1).

$$[(bdt)Mo(O)S_2CuCN]^{2-} + 2e^- = [(bdt)Mo(O)S_2CuCN]^{4-} \quad (1)$$

Finally, the peak current displayed a linear relation to the square root of the scan rate indicating that the active species are molecular in nature and that they function in a diffusion-controlled regime (Fig. S8†).

Cyclic voltammetry of complex 1 in the presence of CO_2 and proton sources

The electroreduction of CO_2 by complex **1** in the absence of a proton source was examined by cyclic voltammetry. Fig. 2 shows the CVs of complex **1** in dry argon- and CO_2-saturated CH_3CN on a GC electrode between -1.52 and -2.62 V. In the presence of CO_2, the redox process at $E_{1/2} = -2.07$ V became irreversible and slightly increased in current density, and a catalytic wave appeared at an onset potential of roughly -2.4 V. The irreversibility and current increase of the signal at -2.07 V was also observed when cycling only down to -2.22 V, before the catalytic wave (inset, Fig. 2).

Further purging the electrochemical cell with argon restored the reversible redox process associated to **1** at -2.07 V, indicating that complex **1** did not decompose in these conditions (Fig. S9†). No products were detected over a 1 hour electrolysis at -2.17 V, confirming the absence of catalytic activity of the complex at that potential. These data suggest a non-catalytic irreversible reaction of reduced complex **1** with CO_2 leading to the formation of the active catalyst. We assigned the slight increase of activity mainly to the increase of concentration of the complex occurring during the CO_2 purging process causing partial evaporation of the solvent.

The effect of proton sources on promoting CO_2 reduction was then investigated. Recording CVs of complex **1** under CO_2

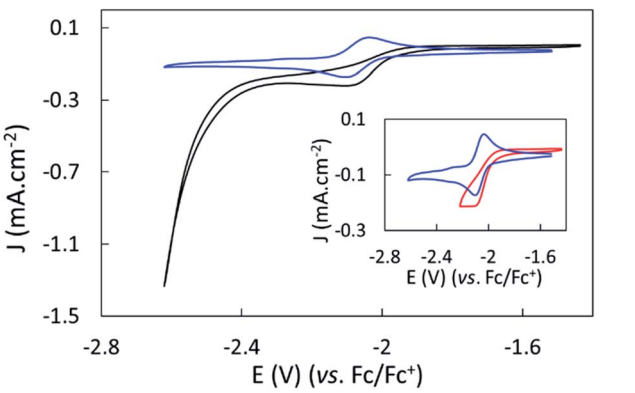

Fig. 2 Cyclic voltammograms of complex **1** under Ar (blue) and CO_2 applying potentials from -1.52 V to -2.22 V *vs.* Fc/Fc^+ (red, inset) and from -1.52 V to -2.62 V *vs.* Fc/Fc^+ (black). 1 mM solution in dry CH_3CN containing 0.1 M $TBAPF_6$ electrolyte; GC working electrode; The scan rate was 50 mV s^{-1}; the second scan is shown.

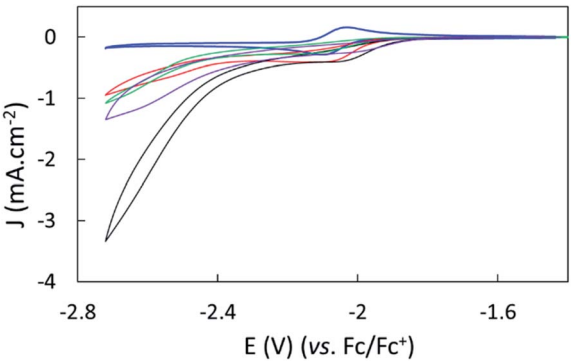

Fig. 3 Cyclic voltammograms of 1 mM complex **1** with 0.1 M $TBAPF_6$ in dry CH_3CN on a GC electrode under Ar (blue), CO_2 (red), CO_2 with 0.1 M TFE (black), CO_2 with 0.1 M H_2O (green) and CO_2 with 0.1 M PhOH (purple). The scan rate was 50 mV s^{-1}; the second scan is shown.

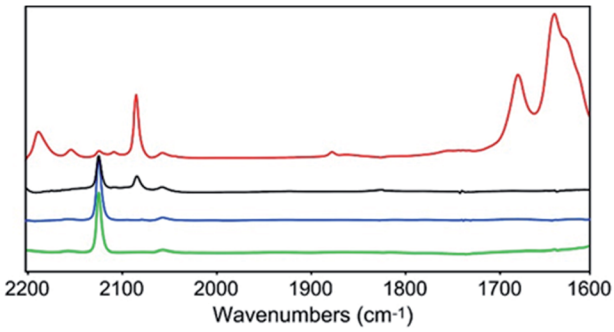

Fig. 4 IR-SEC of complex **1** in dry CH_3CN with 0.1 M $TBAPF_6$ at resting potential under Ar (green), CO_2 (blue), and at −2.24(11) V *vs.* Fc/Fc^+ under Ar (black) and CO_2 (red). LabOMak IR-SEC cell equipped with Pt grid for working and counter electrodes and CE and Ag pseudo-reference electrode.

in the presence of 0.1 M H_2O (green line), 0.1 M TFE (trifluoroethanol, black line) or 0.1 M PhOH (phenol, purple) as proton sources allowed identifying TFE as the most effective to increase the current density of the catalytic process (Fig. 3).The concentration of 0.1 M TFE was found to be optimal, while concentrations greater than 0.2 M resulted in a loss of current density (Fig. S10†).

Catalytic electroreduction of CO_2 studied by controlled potential electrolysis

Controlled potential electrolysis (CPE) was carried out in CO_2-saturated CH_3CN on a GC electrode at −2.62 V in the presence of 0.1 M of TFE. The current density remained stable over the 1 h experiment (Fig. S11†). Product analysis of the headspace by gas chromatography revealed the presence of H_2 and CO as the only gaseous products while ion-exchange liquid chromatography demonstrated the presence of formic acid. Quantification of these products (Table 1) indicated that the major reaction product was formate (FY = 69%), while CO (FY = 8%) and H_2 (FY = 19%) accounted for the rest of the passed charge (total FY = 96%) for an overall turnover number (TON) of 4. A control experiment was carried out under an Ar atmosphere and did not show any formation of CO_2 reduction products, the only detected product being H_2.

The product distribution showed only a minor dependence on the applied potential. When CPE was carried out at a significantly more anodic potential (−2.37 V), FY for formate slightly increased up to 74%, while FY for CO decreased and FY for H_2 remained almost unaffected (Table 1 and Fig. S11†). Control experiment without catalyst showed very low current density and no formate formation (Table 1 and Fig. S12†).

The molecular origin of the catalytically active species was assessed by several control experiments. First, a rinse test was carried out. After 1 hour CPE in the presence of complex **1** under standard catalytic conditions (CO_2-saturated CH_3CN with 0.1 M $TBAPF_6$ and 0.1 M TFE), the electrode was separated from the electrolyte and then assayed for a second CPE using a fresh electrolyte solution in the absence of complex **1**. As shown in Fig. S13,† the current density during the following CPE at −2.62 V was very low, as compared to that observed in the first CPE run, and analysis of the solution after one hour did not show any formation of CO_2 reduction products. Second, no electrodeposited species were observed in electrocatalytic conditions, as shown by the absence of dissolution processes in post-electrolysis CV studies (Fig. S14†) and by the unchanged energy-dispersive X-ray spectra and scanning electron microscopy images of the electrode (Fig. S15–S17†) before and after electrolysis. This suggests that the catalytic activity originates from the soluble molecular species.

The importance of the bimetallic nature of the catalyst was illustrated in a comparative study with the mononuclear bis-bdt Mo complex, $[Mo^{IV}O(bdt)_2][Et_4N]_2$, used as a model of the Mo subunit of complex **1**. The CPE of $[Mo^{IV}O(bdt)_2][Et_4N]_2$ at −2.62 V in CO_2-saturated CH_3CN with 0.1 M $TBAPF_6$ and 0.1 M TFE did not show any CO_2 reduction products (Fig. S18†).

Table 1 Products from controlled potential electrolyses at −2.62 V and −2.37 V *vs.* Fc/Fc^+ during 1 hour on GC electrode[a]

E (V)	Catalyst	FY CO (%)	FY H_2 (%)	FY $HCOO^-$ (%)	Total FY (%)	TON[b]
−2.62	**1** (0.5 mM)	8	19	69	96	2.8 (4.0)[d]
−2.37	**1** (0.5 mM)	4	21	74	99	1.6
−2.62	No catalyst	4	11	0	14[c]	—

[a] 0.1 M $TBAPF_6$ and 0.1 M TFE in 5 mL CO_2-saturated CH_3CN. [b] See ESI for details of turnover number (TON) calculation. [c] The low total FY is a consequence from the very low overall current, rendering background current (faradaic and kinetic/induced background currents) non-negligible. [d] TON after 2 h in brackets.

Infrared spectroelectrochemical studies

In order to gain further insights into the CO_2 reduction reaction mechanism, we investigated the behaviour of complex **1** in the presence of CO_2 *via* an infrared spectroelectrochemistry (IR-SEC) technique (Fig. 4).[39,40] At resting potential, the IR stretch corresponding to the ν_{CN} mode was observed at 2124 cm^{-1} in both Ar and CO_2 atmosphere, confirming that complex **1** did not react with CO_2. At −2.24(11) V, the ν_{CN} mode shifted to 2081 cm^{-1}, in agreement with an increased π backdonation to the CN^- ligand upon reduction. Under a CO_2 atmosphere at −2.24(11) V the same ν_{CN} stretch was observed, together with new stretches at 2150 and 2187 cm^{-1}, indicating the formation of two new complexes presenting a significant change in the geometry of the Cu site. In addition, the appearance of new intense IR bands at 1678 and 1640 cm^{-1}, characteristic of CO_3^{2-} ions, implied that reduced complex **1** reacted with CO_2 *via* oxo-transfer to produce CO_3^{2-} in solution. The complete disappearance of the signal for initial complex **1** at 2124 cm^{-1} highlights the considerably faster kinetics for the complex reduction in presence of CO_2. Finally, the appearance of a new stretch at 1875 cm^{-1} suggested the formation of a Mo–H species.[41] While this stretch was observed in the absence of a proton source, we hypothesize that protons might derive from the acetonitrile solvent. This was further confirmed by the disappearance of this stretch when deuterated acetonitrile was used as a solvent (together with that of the ν_{CN} stretch at 2187 cm^{-1}, likely belonging to the same hydride species, Fig. S19†).

Computational investigations of the CO_2 reduction

DFT computations were performed to explore the CO_2 reduction mechanism by **1** and to further elaborate the assignments of the spectroscopic features discussed above.

Initial reaction of 1 in the presence of CO_2. Complex **1** was fully optimized in CH_3CN starting from its reported X-ray crystal structure.[38] Selected bond distances and angles are summarized in Table S2,† showing excellent agreement with the experimental parameters (bond lengths are within 0.02 Å of the values in the crystal structure and the bond angles are within 1°), except for Mo–Cu/Cu–S bond lengths, which are underestimated by as much as 0.06 Å. The ground state of **1** is a closed-shell singlet, containing Mo^{VI} and Cu^{I} centers, which upon 2-electron reduction generates complex $\mathbf{1}_{red}$ with Mo^{IV} and Cu^{I} sites (see Fig. S20 and S21† for the corresponding frontier molecular orbitals).

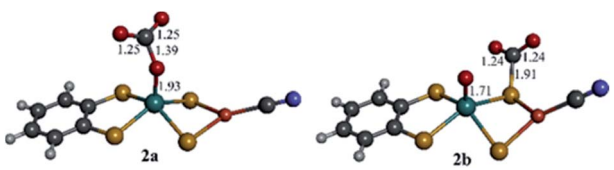

Fig. 5 DFT optimized structures (B3LYP-D3/def2-TZVPD) of CO_2 bound to complex $\mathbf{1}_{red}$ on oxo (**2a**) and on μ_2-S (**2b**). Bond distances are given in Å. Mo is green, Cu is orange, S is yellow, O is red, N is blue, C is grey and H is white.

According to our calculations (Fig. 5), the two most plausible sites for CO_2 binding on the reduced complex $\mathbf{1}_{red}$ are on the oxo atom (complex **2a**) and one of the μ_2-S atoms (complex **2b**), see also Fig. S22 and S23.† The energy difference between the two complexes (B3LYP-D3/def2-TZVPD level) is only 2.8 kcal mol^{-1}. The observation by IR spectroscopy measurements (see above) of CO_3^{2-} species during reaction of reduced complex **1** with CO_2 suggests binding at the Mo=O group and the computed reaction free energy for the generation of complex **2a** is exergonic by 4.5 kcal mol^{-1}. Then, after binding a CO_2 molecule **2a** generates the pre-catalyst **3** ($\Delta G = -0.6$ kcal mol^{-1}) upon an irreversible transfer of the oxo group to form CO_3^{2-} (Fig. 6). Complex **3** has a triplet ground state (the corresponding singlet state is 18.8 kcal mol^{-1} higher in energy), with Mo ion in a tetrahedral geometry.

DFT mechanistic pathways

Electrochemical studies suggest that catalysis requires additional electron(s). Fig. 6 shows the proposed pathways of CO_2 reduction toward formate and hydrogen, involving a further one-electron reduction of **3** leading to $\mathbf{3}_{red}$ complex in a doublet ground state. The associated computed redox potential

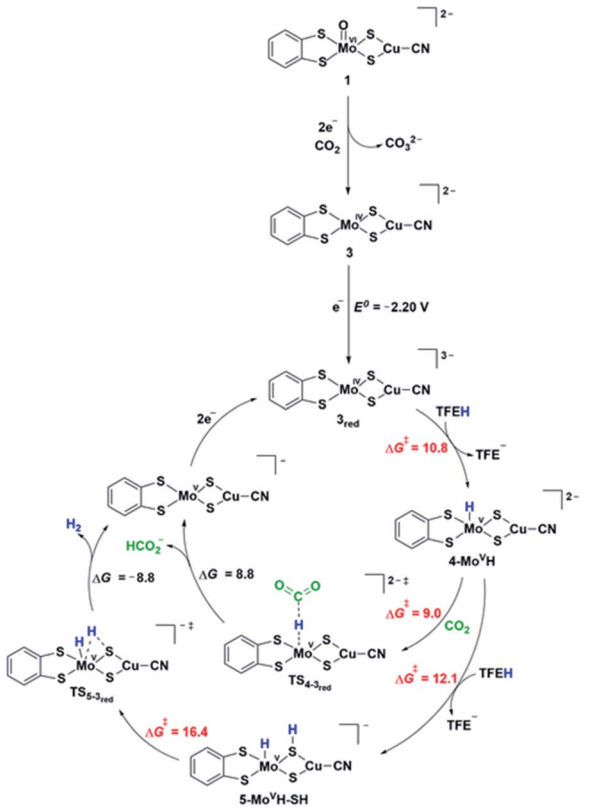

Fig. 6 Proposed reaction mechanisms of CO_2 reduction to formate and hydrogen by complex **3** obtained from the pre-catalyst **1**. The relative Gibbs free energies (ΔG, kcal mol^{-1}) and transition state barriers ($\Delta G^{\#}$, kcal mol^{-1}) are given relative to the preceding intermediate. The standard one-electron reduction potential (E^0, V) is given *vs.* Fc/Fc^+. Note that the added electron in complex $\mathbf{3}_{red}$ resides on the S_{3p} orbitals of the ligands.

($E^0 = -2.20$ V) is in good agreement with the experimental onset of −2.40 V. The added electron resides on the S_{3p} orbitals of the ligands exclusively, thus preserving the oxidation state of Mo^{IV} (Fig. S24b†). Further one-electron reduction of $\mathbf{3_{red}}$ is computed to occur at prohibitive redox potential and, as such, the plausible pathways involving 2-electron reduction of **3** have not been considered. The $\mathbf{3_{red}}$ complex is protonated by a TFE molecule most favorably at the Mo center (computed TS barrier of 10.8 kcal mol^{-1}), giving rise to a Mo hydride species, **4-Mo^{V}H** (Fig. S25†). Alternative protonation of the two different S atom types, *i.e.*, metal bridging S and S from dithiolene, is +4.1 and +16.6 kcal mol^{-1}, respectively, higher in energy. Formate is formed *via* a direct CO_2 attack on **4-Mo^{V}H** through a transition state $\mathbf{TS_{4\text{-}3red}}$ with a free energy of activation of 9 kcal mol^{-1}. Direct hydride transfer to form [$Mo^V\cdots HCO_2^-$] complex is followed by a release of $HCOO^-$ and regeneration of $\mathbf{3_{red}}$ upon two-electron reduction. Alternatively, the **4-Mo^{V}H** intermediate can accept a second proton from the acid source to form **5-Mo^{V}H-SH** ($\Delta G^{\#} = 12.1$ kcal mol^{-1}). The protonation occurs on a bridging S atom, resulting in a S–H bond *syn* to the Mo–H bond. The computed TS barrier for hydrogen formation amounts to 16.4 kcal mol^{-1}. The release of hydrogen (ΔG = −8.8 kcal mol^{-1}) is followed by a two-electron reduction to regenerate the active species $\mathbf{3_{red}}$. In contrast, a direct attack of TFE on the Mo–H bond to form MoH_2 adduct has a significantly higher transition state barrier of 28.7 kcal mol^{-1} and is hence ruled out as an operating H_2 pathway.

IR frequencies by DFT

The reaction mechanism in Fig. 6 is further corroborated by comparison of computed characteristic vibrational frequencies of complex **1** and some of the key intermediates in the catalytic cycle to the experimental IR-SEC vibrations (Tables S3 and S4†). The experimental ν_{CN} stretches at 2081 cm^{-1}, 2150 cm^{-1} and 2187 cm^{-1} observed upon reduction of complex **1** in a CO_2 atmosphere are in good agreement with the computed values at 2059, 2128, and 2135 cm^{-1} of the reduced complexes $\mathbf{1_{red}}$, **3** and **4-Mo^{V}H**. Moreover, the calculated Mo–H stretching mode at 1858 cm^{-1} strongly suggests that the measured band at 1874 cm^{-1} can be attributed to the hydride complex **4-Mo^{V}H** formed in the presence of a proton source, which is a key intermediate for the product formation.

Discussion and conclusions

The main goal of this work was to evaluate the electrocatalytic activity in CO_2 reduction of the heterobimetallic complex [(bdt)$Mo^{VI}(O)S_2Cu^{I}CN]^{2-}$, **1**, which is inspired by the active site of the CODH2 enzyme. We found that complex **1** was catalytically active and shows a good selectivity for formate, formed with an overpotential of *ca.* 800 mV. Such high overpotentials have been often observed for the few molecular catalysts catalyzing the reduction of carbon dioxide to formate.[1,42]

Combined electrochemical analysis, IR-SEC data, DFT computations and catalytic activity studies identified that complex **1** is only a pre-catalyst. Its two-electron reduction triggers the irreversible transfer of the oxo group on Mo to a CO_2 molecule to afford one carbonate equivalent and the tetrahedral Mo(IV) complex **3**. The mechanism for the oxo transfer observed here differs significantly from oxo-transfer mechanisms observed with molybdoenzymes and synthetic analogues,[43] where the oxo transfer is a redox process involving the reduction of a dioxo Mo(VI) complex to a monooxo Mo(VI) species. In the present case, the monooxo Mo(VI) complex **1** has only a weak basic character and the 2-electron reduction of the Mo center allows lowering its Lewis acidity and sufficiently enhancing the basicity of the oxo group to induce its transfer to CO_2. The resulting complex, **3**, can be further reduced by one electron to generate the active catalyst $\mathbf{3_{red}}$, which is showing strong electron-donating properties at the Mo center provided by the metal-bridging S ligands. This allows for the formation of reactive Mo^VH hydride intermediates, which can react with CO_2 to produce formate. The rather large overpotential observed with this catalyst can be explained by the highly cathodic potential required to transfer an electron on the S_{3p}, necessary to generate a hard Mo center able to react with TFE and form such Mo^VH hydride intermediates. Furthermore, the higher transition state barrier for hydrogen formation than the barrier for formate production of these Mo hydride species is in agreement with the experimental finding of formate being the major product, while H_2 accounts for only 20%.

This work enriches the family of CO_2-to-formate electrocatalysts based on earth-abundant metals. The generation of an active CO_2 reduction catalyst species *via* the loss of an oxo group involved in carbonate formation is to our knowledge unprecedented. It allows for an *in situ* generation of a vacant coordination site leading to the formation of a highly reactive metal hydride complex. The presence of the Cu^I site is essential for the catalytic function of this catalyst, but more efforts are needed to understand the interplay between the two metal centers, which will be a subject of future studies.

Experimental section

General methods

All experiments were performed under dry and oxygen-free argon atmosphere using standard Schlenk or glovebox techniques. Unless otherwise specified, solvents were dried using a MBRAUN SPS-800 solvent purification system. Diethyl ether was vacuum distilled from K/benzophenone. All solvents were degassed by three freeze–pump–thaw cycles prior to use. Acetonitrile was stored over activated 3 Å molecular sieves and diethyl ether and dichloromethane were stored over 4 Å molecular sieves. Water solutions were prepared from distilled and degassed MilliQ water. ^{1}H NMR spectra were recorded on a Bruker Avance-III 300 MHz NMR spectrometer at room temperature. UV-Vis spectra were recorded using a Cary 100 UV-Vis spectrophotometer (Agilent). FTIR spectroscopy measurements were carried out in a glovebox using a Nicolet iS5 instrument from Thermo Scientific. SEM measurements were acquired using a SEM-FEG Hitachi SU-70 scanning electron microscope. The complex $[Mo^{IV}O(bdt)_2][Et_4N]_2$ was prepared according to literature procedures.[44,45]

Synthesis of $(Et_4N)_2[(bdt)Mo^{VI}(O)S_2Cu^{I}CN]$, (1)

In the glovebox, a 5 mL acetonitrile solution of 1,2-benzenedithiol (0.042 g, 0.29 mmol) was added under stirring to an orange solution of $(Et_4N)_2[O_2MoS_2CuCN]$ (0.158 g, 0.29 mmol) in 15 mL acetonitrile. The solution immediately turned purple-black. Stirring was pursued for 4 hours. Solvent was removed under vacuum, and the purple-black solid was washed with diethyl ether (3 × 5 mL) to afford a purple powder. Recrystallization from acetonitrile/diethyl ether yielded ($(Et_4N)_2$[**1**]) as purple crystals (0.149 g, 76%). IR (cm^{-1}) (intensity): ν(CN) 2119 (medium), ν(Mo=O) 916 (strong). UV-Vis (λ_{max}, nm, CH_3CN): 233, 251, 310, 380, 528. ^1H NMR (CD_3CN, anion): δ 7.30 (dd, 2H), 6.81 (dd, 2H).

Electrochemistry

All cyclic voltammetry (CV) and bulk electrolysis experiments were performed using a gastight three-electrode single-compartment cell with a SP300 Bio-Logic potentiostat (Bio-Logic Science instruments SAS). Solutions (for CV and CPE) were prepared in the glove box with dry and degassed acetonitrile (CH_3CN), 0.1 M tetrabutylammonium hexafluorophosphate ($TBAPF_6$) as the supporting electrolyte and 1 mM of the studied complex unless specified. 3 M Ag/AgCl electrodes, using a guard filled with the electrolyte solution and separated from the cell by a Vycor frit was used as the reference electrode unless specified.

For CV studies, the electrochemical cell (SVC-2 Voltammetry cell, ALS Co., Japan) was loaded in glovebox before the experiments. A 0.5 mm diameter platinum wire (5 cm length) was used as the counter electrode. 1 mm diameter glassy carbon electrode (BASi, USA) was used as the working electrode. The scan rate was 50 mV s^{-1} unless specified. In all CV plots reported in this work the 2nd scan is presented. Experiments were run outside the glovebox after further purging the cell with Ar or CO_2 for a minimum of 20 minutes. Ferrocene was used as an internal standard in each experiment by addition to the cell at the end of the measurement and running a subsequent CV cycle.

Bulk electrolysis experiments were performed using a gastight custom-built H-type cell loaded in a glovebox with its two compartments separated by two Ceramic-PVDF composite membranes (16 μm thickness, Xuran). A 0.5 mm diameter platinum wire (10 cm length) was used as the counter electrode and placed in the anodic compartment. A glassy carbon electrode plate (2 cm^2, 1 mm thickness, Alfa Aesar) was used as the working electrode in the cathodic compartment. The cell was purged with Ar or CO_2 for a minimum of 30 minutes before controlled potential electrolysis would be carried out. Faradaic efficiencies were calculated accounting for the two equivalents of electrons initially required to generate the catalyst from complex **1**.

Infrared spectroelectrochemistry (IRSEC)

Infrared spectroelectrochemistry (IR-SEC) experiments were performed using 10 mM solution of the complex in CH_3CN containing 0.1 M $TBAPF_6$ as supporting electrolyte. The experiments were carried out in a LabOMak UF SEC cell with Pt mesh working and counter electrode. Unless otherwise stated, FTIR spectra were recorded after a constant potential electrolysis of 20 s at −1.9 V *vs.* a Ag wire pseudo reference electrode and were refereed to Fc/Fc^+ by measuring the reversible potential of Fc added in the IR-SEC cell in the last cycle of the measurement sequence. Small shifts of potential (in the range of 200 mV) for the Fc/Fc^+ couple were occasionally observed in our setup and for the first CV cycle before stabilizing (Fig. S26†). To account for these small potential shifts, all IR-SEC experiments were referenced to the value of +0.34 V, which is the average $E_{1/2}$ for Fc/Fc^+ determined in our setup for the experiments reported here and provided the associated standard deviation value of 0.11 V in the text.

Product detection

H_2 and CO were analyzed by gas chromatography (Multi-Gas Analyzer #5; SRI Instruments), equipped with HaySep D and MoleSieve 5 Å columns and thermal conductivity detector and flame ionization detector equipped with a methanizer using argon as a carrier gas. The gas chromatograph was calibrated by using a standard gas mixture containing 2500 ppm of H_2 and CO in CO_2 (Messer). The typical volume of injected gas was 50 μL.

Formate was quantified using ion exchange chromatography (883 Basic IC; Metrohm).

Computational details

All geometries were fully optimized at the B3LYP-D3 [46–49]/def2-TZVPD[50,51] level of density functional theory using the Gaussian 09 software package[52] and the SMD implicit-solvation model (ε = 35.688 for acetonitrile).[53] A quasi-relativistic SDD pseudopotential was used for Mo.[54] Harmonic vibrational frequencies were computed on the optimized geometries to ensure that all local minima display real frequencies only, whereas the transition states were characterized by a single imaginary frequency. Thermochemical contributions were calculated using the ideal gas, rigid rotor, and harmonic oscillator approximations at a temperature of 298.15 K. The activation barriers were computed using TFE molecule as an explicit proton source. The reduction potentials were calculated using the relation $E^0 = (-\Delta G^0/nF) - E^0_{ref}$, in which n is the number of transferring electrons, F is Faraday's constant, ΔG^0 is the Gibbs free energy of reduction, calculated for structures optimized in solution, and E^0_{ref} is the absolute reduction potential of the reference species (Fc/Fc^+ couple) computed at the same level of theory.

Conflicts of interest

There are no conflicts to declare.

Acknowledgements

The authors warmly thank Dr Françoise Pillier for help with SEM measurements, and Dr David Wakerley for valuable assistance for electrochemical measurements and analyses. This work was supported by the ANR JCJC project NitroCOCa

(ANR-17-CE05-0021). The calculations were performed using the HPC resources of GENCI (TGCC) through Grant 2019-810082.

Notes and references

1 R. Francke, B. Schille and M. Roemelt, *Chem. Rev.*, 2018, **118**, 4631–4701.
2 N. Elgrishi, M. B. Chambers, X. Wang and M. Fontecave, *Chem. Soc. Rev.*, 2017, **46**, 761–796.
3 C. Costentin, M. Robert and J.-M. Savéant, *Chem. Soc. Rev.*, 2013, **42**, 2423–2436.
4 W. W. Kramer and C. C. L. McCrory, *Chem. Sci.*, 2016, **7**, 2506–2515.
5 X. Wang, I. Thiel, A. Fedorov, C. Copéret, V. Mougel and M. Fontecave, *Chem. Sci.*, 2017, **8**, 8204–8213.
6 C. Sun, L. Rotundo, C. Garino, L. Nencini, S. S. Yoon, R. Gobetto and C. Nervi, *ChemPhysChem*, 2017, **18**, 3219–3229.
7 B. Reuillard, K. H. Ly, T. E. Rosser, M. F. Kuehnel, I. Zebger and E. Reisner, *J. Am. Chem. Soc.*, 2017, **139**, 14425–14435.
8 A. Zhanaidarova, C. E. Moore, M. Gembicky and C. P. Kubiak, *Chem. Commun.*, 2018, **54**, 4116–4119.
9 M. N. Jackson, S. Oh, C. J. Kaminsky, S. B. Chu, G. Zhang, J. T. Miller and Y. Surendranath, *J. Am. Chem. Soc.*, 2018, **140**, 1004–1010.
10 S. Sato, K. Saita, K. Sekizawa, S. Maeda and T. Morikawa, *ACS Catal.*, 2018, **8**, 4452–4458.
11 A. Zhanaidarova, A. L. Ostericher, C. J. Miller, S. C. Jones and C. P. Kubiak, *Organometallics*, 2019, **38**, 1204–1207.
12 A. Zhanaidarova, S. C. Jones, E. Despagnet-Ayoub, B. R. Pimentel and C. P. Kubiak, *J. Am. Chem. Soc.*, 2019, **141**, 17270–17277.
13 D. Karapinar, A. Zitolo, T. N. Huan, S. Zanna, D. Taverna, L. H. G. Tizei, D. Giaume, P. Marcus, V. Mougel and M. Fontecave, *ChemSusChem*, 2020, **13**, 173–179.
14 M. Beley, J. P. Collin, R. Ruppert and J. P. Sauvage, *J. Am. Chem. Soc.*, 1986, **108**, 7461–7467.
15 M. Beley, J.-P. Collin, R. Ruppert and J.-P. Sauvage, *J. Chem. Soc., Chem. Commun.*, 1984, 1315–1316.
16 M. Wang, K. Torbensen, D. Salvatore, S. Ren, D. Joulié, F. Dumoulin, D. Mendoza, B. Lassalle-Kaiser, U. Işci, C. P. Berlinguette and M. Robert, *Nat. Commun.*, 2019, **10**, 1–8.
17 M. Hammouche, D. Lexa, J. M. Savéant and M. Momenteau, *J. Electroanal. Chem. Interfacial Electrochem.*, 1988, **249**, 347–351.
18 M. Bourrez, F. Molton, S. Chardon-Noblat and A. Deronzier, *Angew. Chem., Int. Ed.*, 2011, **50**, 9903–9906.
19 C. Cometto, L. Chen, P.-K. Lo, Z. Guo, K.-C. Lau, E. Anxolabéhère-Mallart, C. Fave, T.-C. Lau and M. Robert, *ACS Catal.*, 2018, **8**, 3411–3417.
20 M. D. Rail and L. A. Berben, *J. Am. Chem. Soc.*, 2011, **133**, 18577–18579.
21 S. Roy, B. Sharma, J. Pécaut, P. Simon, M. Fontecave, P. D. Tran, E. Derat and V. Artero, *J. Am. Chem. Soc.*, 2017, **139**, 3685–3696.
22 S. Dey, M. E. Ahmed and A. Dey, *Inorg. Chem.*, 2018, **57**, 5939–5947.
23 A. Taheri, E. J. Thompson, J. C. Fettinger and L. A. Berben, *ACS Catal.*, 2015, **5**, 7140–7151.
24 A. M. Appel, J. E. Bercaw, A. B. Bocarsly, H. Dobbek, D. L. DuBois, M. Dupuis, J. G. Ferry, E. Fujita, R. Hille, P. J. A. Kenis, C. A. Kerfeld, R. H. Morris, C. H. F. Peden, A. R. Portis, S. W. Ragsdale, T. B. Rauchfuss, J. N. H. Reek, L. C. Seefeldt, R. K. Thauer and G. L. Waldrop, *Chem. Rev.*, 2013, **113**, 6621–6658.
25 T. Fogeron, P. Retailleau, L.-M. Chamoreau, Y. Li and M. Fontecave, *Angew. Chem., Int. Ed.*, 2018, **57**, 17033–17037.
26 J.-P. Porcher, T. Fogeron, M. Gomez-Mingot, E. Derat, L.-M. Chamoreau, Y. Li and M. Fontecave, *Angew. Chem., Int. Ed.*, 2015, **54**, 14090–14093.
27 T. Fogeron, J.-P. Porcher, M. Gomez-Mingot, T. K. Todorova, L.-M. Chamoreau, C. Mellot-Draznieks, Y. Li and M. Fontecave, *Dalton Trans.*, 2016, **45**, 14754–14763.
28 J.-P. Porcher, T. Fogeron, M. Gomez-Mingot, L.-M. Chamoreau, Y. Li and M. Fontecave, *Chem.–Eur. J.*, 2016, **22**, 4447–4453.
29 T. Fogeron, P. Retailleau, L.-M. Chamoreau, M. Fontecave and Y. Li, *Dalton Trans.*, 2017, **46**, 4161–4164.
30 T. Fogeron, T. K. Todorova, J.-P. Porcher, M. Gomez-Mingot, L.-M. Chamoreau, C. Mellot-Draznieks, Y. Li and M. Fontecave, *ACS Catal.*, 2018, **8**, 2030–2038.
31 T. Fogeron, P. Retailleau, M. Gomez-Mingot, Y. Li and M. Fontecave, *Organometallics*, 2019, **38**, 1344–1350.
32 J.-H. Jeoung and H. Dobbek, *Science*, 2007, **318**, 1461–1464.
33 H. Dobbek, L. Gremer, R. Kiefersauer, R. Huber and O. Meyer, *Proc. Natl. Acad. Sci. U. S. A.*, 2002, **99**, 15971–15976.
34 C. Gourlay, D. J. Nielsen, J. M. White, S. Z. Knottenbelt, M. L. Kirk and C. G. Young, *J. Am. Chem. Soc.*, 2006, **128**, 2164–2165.
35 C. Gourlay, D. J. Nielsen, D. J. Evans, J. M. White and C. G. Young, *Chem. Sci.*, 2018, **9**, 876–888.
36 S. Groysman, A. Majumdar, S.-L. Zheng and R. H. Holm, *Inorg. Chem.*, 2010, **49**, 1082–1089.
37 T. S. Hollingsworth, R. L. Hollingsworth, R. L. Lord and S. Groysman, *Dalton Trans.*, 2018, **47**, 10017–10024.
38 M. Takuma, Y. Ohki and K. Tatsumi, *Inorg. Chem.*, 2005, **44**, 6034–6043.
39 C. W. Machan, M. D. Sampson, S. A. Chabolla, T. Dang and C. P. Kubiak, *Organometallics*, 2014, **33**, 4550–4559.
40 Q. Zeng, J. Tory and F. Hartl, *Organometallics*, 2014, **33**, 5002–5008.
41 H. D. Kaesz and R. B. Saillant, *Chem. Rev.*, 1972, **72**, 231–281.
42 H. Takeda, C. Cometto, O. Ishitani and M. Robert, *ACS Catal.*, 2017, **7**, 70–88.
43 J. H. Enemark, J. J. A. Cooney, J.-J. Wang and R. H. Holm, *Chem. Rev.*, 2004, **104**, 1175–1200.
44 A. Roodt, S. S. Basson and J. G. Leipoldt, *Polyhedron*, 1994, **13**, 599–607.
45 S. Boyde, S. R. Ellis, C. D. Garner and W. Clegg, *J. Chem. Soc., Chem. Commun.*, 1986, 1541–1543.
46 A. D. Becke, *J. Chem. Phys.*, 1993, **98**, 5648–5652.

47 P. J. Stephens, F. J. Devlin, C. F. Chabalowski and M. J. Frisch, *J. Phys. Chem.*, 1994, **98**, 11623–11627.
48 S. Grimme, J. Antony, S. Ehrlich and H. Krieg, *J. Chem. Phys.*, 2010, **132**, 154104.
49 S. Grimme, S. Ehrlich and L. Goerigk, *J. Comput. Chem.*, 2011, **32**, 1456–1465.
50 F. Weigend and R. Ahlrichs, *Phys. Chem. Chem. Phys.*, 2005, **7**, 3297–3305.
51 D. Rappoport and F. Furche, *J. Chem. Phys.*, 2010, **133**, 134105.
52 M. J. Frisch, G. W. Trucks, H. B. Schlegel, G. E. Scuseria, M. A. Robb, J. R. Cheeseman, G. Scalmani, V. Barone, B. Mennucci, G. A. Petersson, *et al.*, *Gaussian 09*, Gaussian, Inc., Wallington CT., 2013.
53 A. V. Marenich, C. J. Cramer and D. G. Truhlar, *J. Phys. Chem. B*, 2009, **113**, 6378–6396.
54 D. Andrae, U. Häußermann, M. Dolg, H. Stoll and H. Preuß, *Theor. Chim. Acta*, 1990, **77**, 123–141.